Chapter 10
The Construction of a Highway Fieldtest Section for Vehicle–Road Interaction

The interaction between a heavy truck and a road system is theoretically studied in the previous chapters. However, field tests of both vibration performance of the vehicle and the road system response have been very few due to the limitation of technical conditions. In order to study further the interaction between a vehicle and the pavement, to master the failure pattern of the road structure under vehicle loads, to improve vehicle driving safety and to verify the theoretical analysis and numerical simulations, a field test section for vehicle–road interaction was built on the ShenZhou to DaMing segment of the DaGuang (Daqing to Guangzhou) highway. The field test of vehicle random dynamic load response and road dynamic response were conducted.

10.1 The Experiment Scheme of the Vehicle–Road System

For the study of the interaction between vehicles and a road structure, various kinds of sensors in every layer of the test section are embedded and some sensors are installed in the tested vehicle. Under different axle load conditions (weight empty, half load, or full load) and various vehicle speeds (10, 20, 30, 40, 50, 60 km/h), the responses of the vehicle and the road system are recorded simultaneously. The speed of each point on the vehicle, the dynamic pressure, static pressure, the longitudinal and transverse dynamic strain data of the road's different layers are all collected. These data are long-term remotely monitored and collected in long-term to study the dynamic response rules of each structural layer of the road during the highway operation.

S. Yang et al., *Dynamics of Vehicle-Road Coupled System,*
DOI 10.1007/978-3-662-45957-7_10

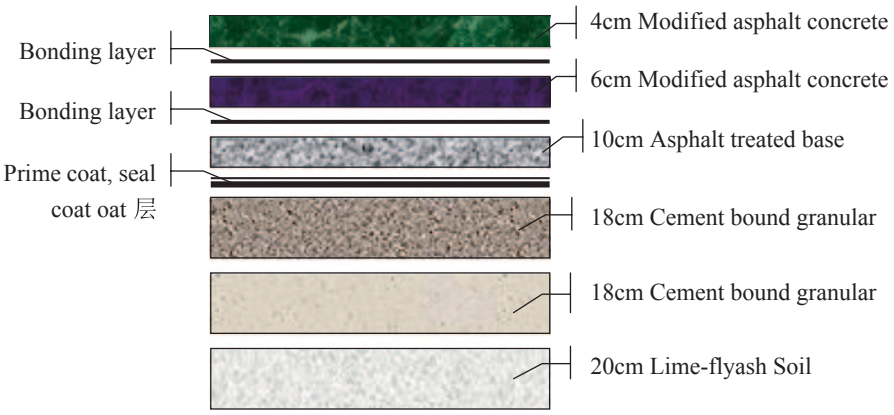

Fig. 10.1 Road structure and material design

10.2 The Highway Field Test System

10.2.1 Introduction of the Highway Road Structure

The total length of the trial section chosen from ShenZhou to DaMing of the DaGuang highway is 220.429 km, 33.4 km of which is expanded as a two-way six-lane highway. The structure scheme of the road is summarized as below: the total width of the roadbed is 34.5 m, in which the width of a one-way lane is 3 × 3.75 m, the width of the middle strip is 4.5 m (including 3 m central dividing strip and two 0.75 m curbs), the paved shoulder is 3.0 m (including 0.5 m width curb), and the soil shoulder width is 0.75 m. The road structure and material design is shown in Fig. 10.1.

10.2.2 The Testing System of the Road

Targeting the problem of fatigue cracking in asphalt pavement, the strain transducer is used for real-time dynamic monitoring of pavement strain. The transverse strain sensors and the longitudinal strain sensors are installed at the bottom of a modified asphalt AC layer, coated macadam, and cement stabilized macadam. Considering the need for comparative analysis, two rows of transverse strain sensors and longitudinal strain sensors are symmetrically laid along the center of the vehicle load track. In order to evaluate the stress of the road structure layers effectively, dynamic and static pressure sensors are embedded in each layer [1, 2].

1. The strain sensor

Along the center line of the tire, the transverse and the longitudinal strain sensors are buried at the bottom of a modified asphalt concrete and asphalt treated base, forming the transverse and longitudinal strain test matrix. These sensors are used for monitoring the longitudinal and transverse strain of the road.

2. The load sensor

The dynamic pressure sensors are embedded successively at the bottom of a modified asphalt concrete layer, asphalt treated base, cement bound granular and on the top of the soil base, which are used for testing the vertical dynamic stress of each layer. The static pressure sensors are set on the top of the soil base to test the vertical static pressure.

The total length of the test road is 100 m and the sensors of each pavement layer and signal acquisition system are shown in Fig. 10.2.

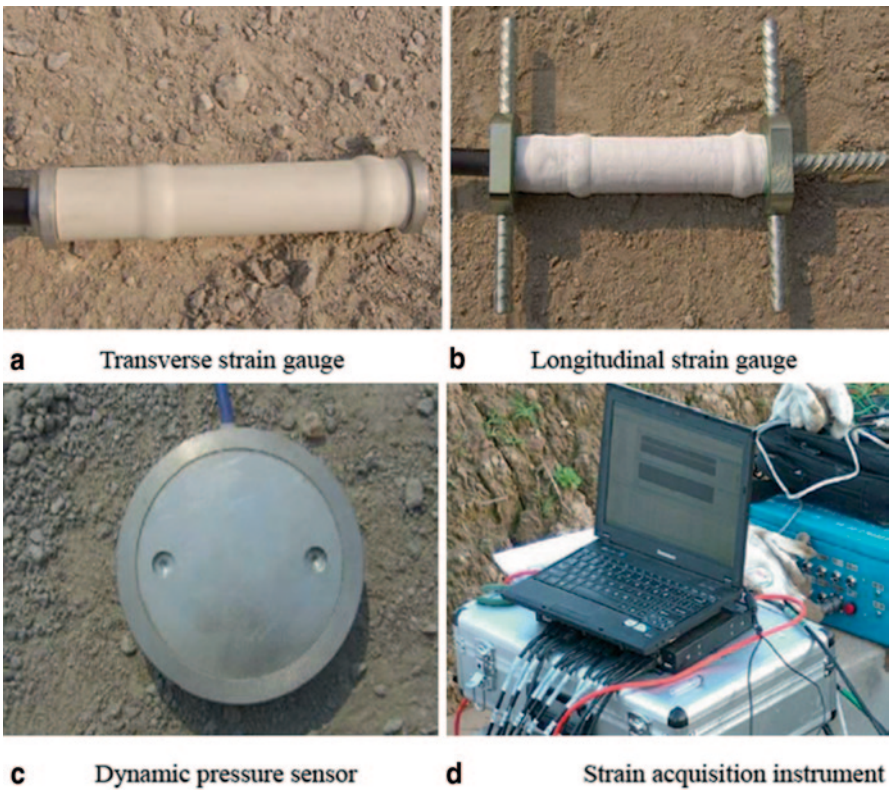

Fig. 10.2 Pavement sensor and signal acquisition analyzer. **a** Transverse strain gauge. **b** Longitudinal strain gauge. **c** Dynamic pressure sensor. **d** Strain acquisition instrument

The signal acquisition system for strain utilizes the Beijing Andy Iotech strain collection device which includes a high performance, multichannel parallel data collection and analysis system. The device includes 48 channels, which can carry out long, continuous data collection (sampling frequency at 1600 Hz). When a vehicle is traveling on the road surface, the computer can record all sensors' electric signals simultaneously. The signals are then transformed to a dynamic strain wave of the measuring point.

10.2.3 The Laying Process of the Sensor

During the construction of each layer of the highway, some sensors are placed at the structure layers in accordance with the design drawing simultaneously, which can ensure the reliability of the data, and also reflect the road dynamic response of every layer [3]. Based on the coring specimens collected at the site, the road physical parameters of each layer are obtained through laboratory experiments. The calibration site and sampling process of the road parameter are shown in Fig. 10.3

On the basis of large-scale research and investigation [4–7] the specific process of laying out the sensors is listed as follows:

1. Calibration of the sensor installation position

In the process of sensor installation, the position of the vehicle wheel tracks is determined to identify each sensor's position relative to the wheel track line. The sensors are embedded in sequence from the subbase to the surface layer of the road. The measuring instruments are used to assist positioning and make the benchmark strict.

2. Overall layout and circuit layout

Due to the large quantity, the various types of sensors, and the high standards of the sensors, the embedding scheme must be designed in advance before the compaction

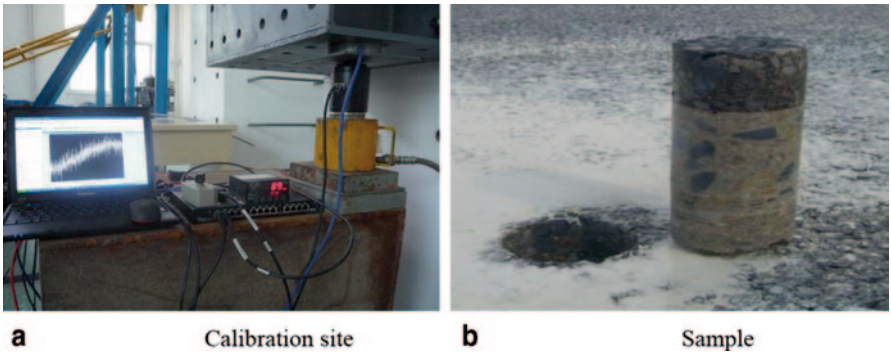

Fig. 10.3 **a** Calibration site. **b** Sample

of the road structure. The embedding position and direction of the sensor should be checked to make sure the arrangement of the sensors' circuit is reasonable. It can reduce unnecessary loss in the process of sensor installation.

3. Artificial digging and circuit slotting

After determining the sensor location, a Luoyang shovel is used to dig the holes, then the circuit is slotted along with the mark. The holes must be dug according to the sensor embedded scheme. It can ensure the precision of the data acquisition.

4. Sensor placement and debugging

The influence of coefficient of loose paving material should be taken into account. A layer of the same mixture dug is covered at the bottom of the hole. Due to the sensibility of the surrounding environment and the fragile structure of the sensors, direct use of mechanical compaction is prone to damage the sensors, destroy the circuits, or lead to other issues. So it is necessary to use the method of artificial ramming preloading. The buried sensors are preliminarily debugged to observe whether the transmission of the signal is normal and to examine the survival rate of the sensor simultaneously.

5. Mechanical paving and compaction

After the completion of artificial ramming preloading of the sensors, the mechanical paving and compaction of the upper structure construction is carried out in accordance with the road construction schedule requirements. To ensure the effect of compaction, the original structure layer must be repeatedly compacted using the rolling machinery. A technician is assigned to protect the wire connector in order to avoid sensor damage by the paving compaction machinery.

6. Wire connector labeled

The initial arrangement of the sensors is finished after the mechanical paving rolling. At this time, sensors are categorized, packaged, and waterproofed to adapt to the requirements of long-term acquisition work.

The installation, connection, and debugging process of the sensors on the scene is shown in Fig. 10.4:

In this experiment, there is an inspection chamber equipped with instruments near the road test section. It not only allows the researchers to connect the instrument of each section to all the test sections on the shared data acquisition system, but also can guarantee the sensor connectors are dry, clean, and easy to identify. The inspection chamber is shown in Fig. 10.5.

Fig. 10.4 Sensor layout process. **a** Location. **b** Digging. **c** Wiring. **d** Placement. **e** Preliminary debugging. **f** Mechanical paving

Fig. 10.5 Inspection chamber

10.3 Vehicle Test System

10.3.1 Introduction of the Vehicle System

On the investigation basis of the traffic in our country at present, a Dongfeng medium-sized truck with three axles is selected as a typical domestic transportation vehicle. There are three types of working conditions: empty load, half load, and full load. In the experimental stage, the vehicle axle load is under strict control to ensure the reliability of the test results.

10.3.2 Introduction of Vehicle Test System

The vehicle test signal acquisition system mainly includes a three-speed sensor, a charge amplifier, a signal acquisition instrument, and a computer [8]. The TSC-D3 speed sensor produced by Chengdu Zhongke Measurement and Control Co., LTD is operated in the 1–500 Hz frequency range. The signal acquisition instrument converts the piezoelectric signals into digital signals. The INV360DF intelligent acquisition analyzer is produced by Beijing Orient Institute of Noise & Vibration. The testing site and collection device is shown in Fig. 10.6.

Figures 10.7–10.10 show each velocity measuring point sensor arrangement on the driver's seat, front steering axle head, intermediate axle head, and rear axle head, respectively.

Fig. 10.6 Testing site and collection device

Fig. 10.7 Driver's seat

Fig. 10.8 Front steering axle head

Fig. 10.9 Intermediate axle head

Fig. 10.10 Rear axle head

10.4 Analysis of the Road Test Results

10.4.1 Analysis of Road Dynamic Strain Response

1. Road dynamic strain under different vehicle speeds

It is discovered from the large amount of measured data that the longitudinal and the transverse flexural strains at the bottom of asphalt concrete show alternation between tensile and compressive strain states under different vehicle axle loads and speeds.

Under the condition of a full load and a speed of 10 km/h, the test result of longitudinal strain of the bottom surface is shown in Fig. 10.11. Under the condition of a full load and a speed of 60 km/h, the test result of the transverse strain at the bottom of the surface layer is shown in Fig. 10.13. The finite element model from chapter two is used to obtain the simulation results; the longitudinal and the transverse strains of the bottom are shown in Figs. 10.12 and 10.14, respectively.

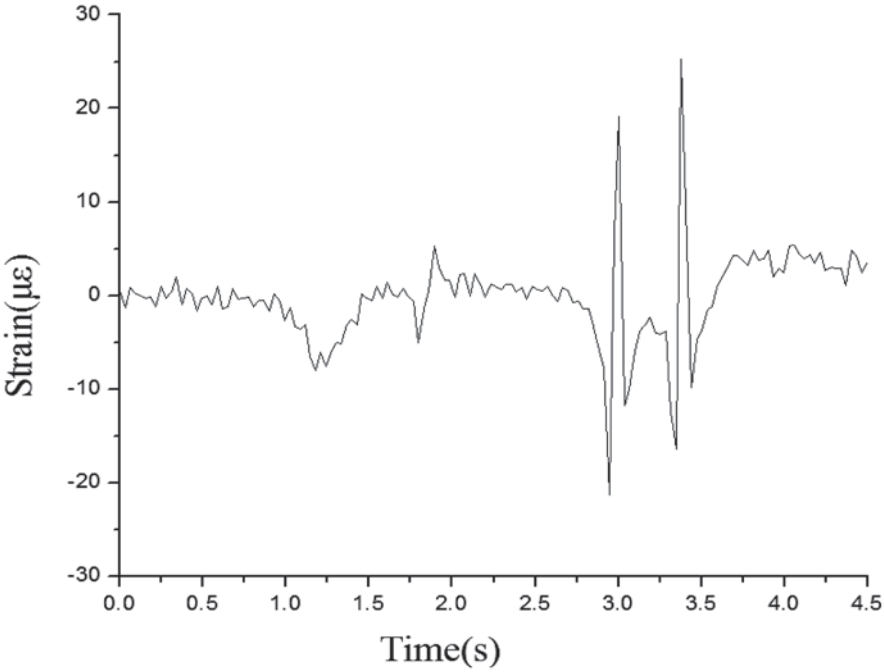

Fig. 10.11 Longitudinal tensile strain at the bottom of asphalt concrete (experiment)

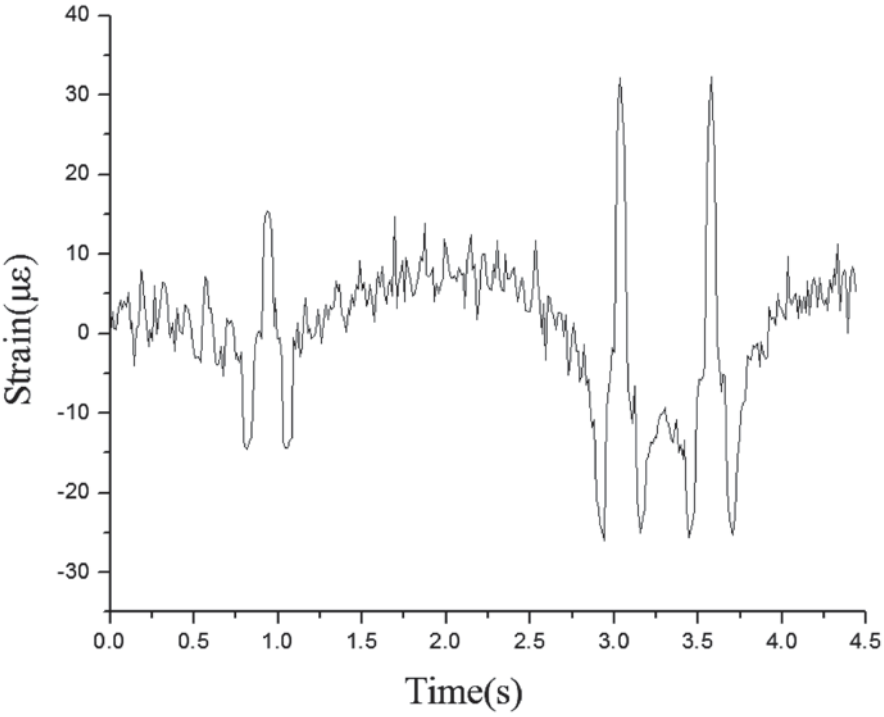

Fig. 10.12 Longitudinal tensile strain at the bottom of asphalt concrete (simulation)

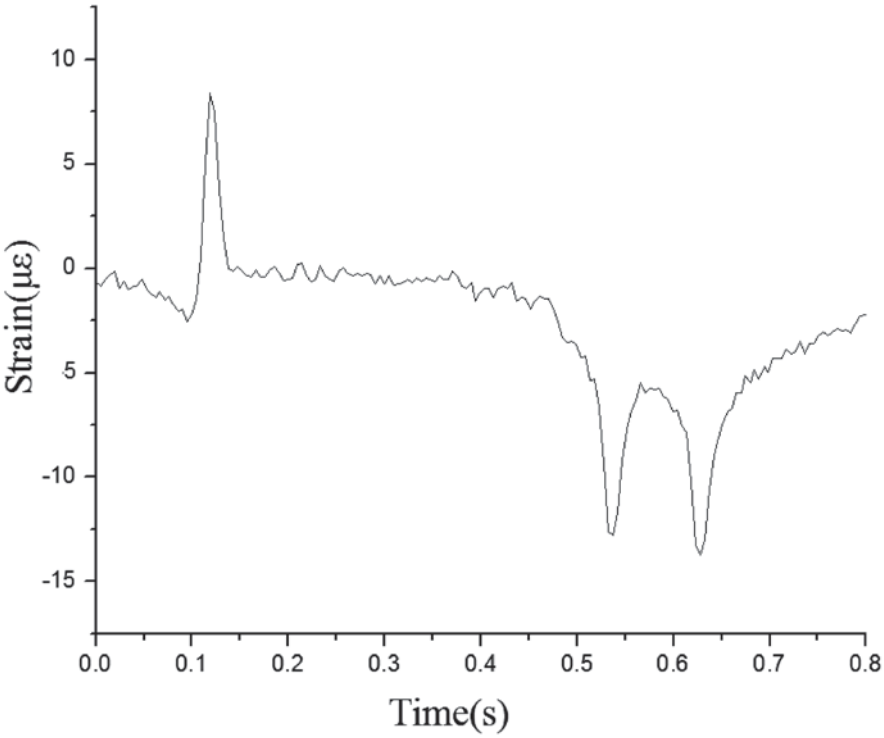

Fig. 10.13 Transverse tensile strain at the bottom of asphalt concrete (experiment)

From Figs. 10.11–10.14, it can be observed that:

1. When the wheels arrive at and leave a point on the pavement, the longitudinal strain at the bottom of the asphalt concrete layer is negative. When the wheels just go past the point, the longitudinal strain becomes positive. This indicates that the asphalt concrete layer mainly bears the longitudinal tensile strain coming from the wheel loading. The conclusion is consistent with the results of previous researcher [9–11].The transverse strain at the bottom of the asphalt concrete includes both tensile strain and compressive strain and the behavior is more complex.
2. The maximum values of the test results of the longitudinal and the transverse tensile strains at the bottom of the asphalt concrete are 26.3 με and13.8 με respectively. The simulation results are 31.9 με, 17.1 με and the relative error is 21.3 %, 23.2 %. The results between the experiment and the simulation are consistent.

Under the condition of a full load at different vehicle speeds, the maximum longitudinal and the transverse tensile strains of the road surface are shown in Fig. 10.14. Figure 10.15 shows that, with an increase in speed, the longitudinal and the

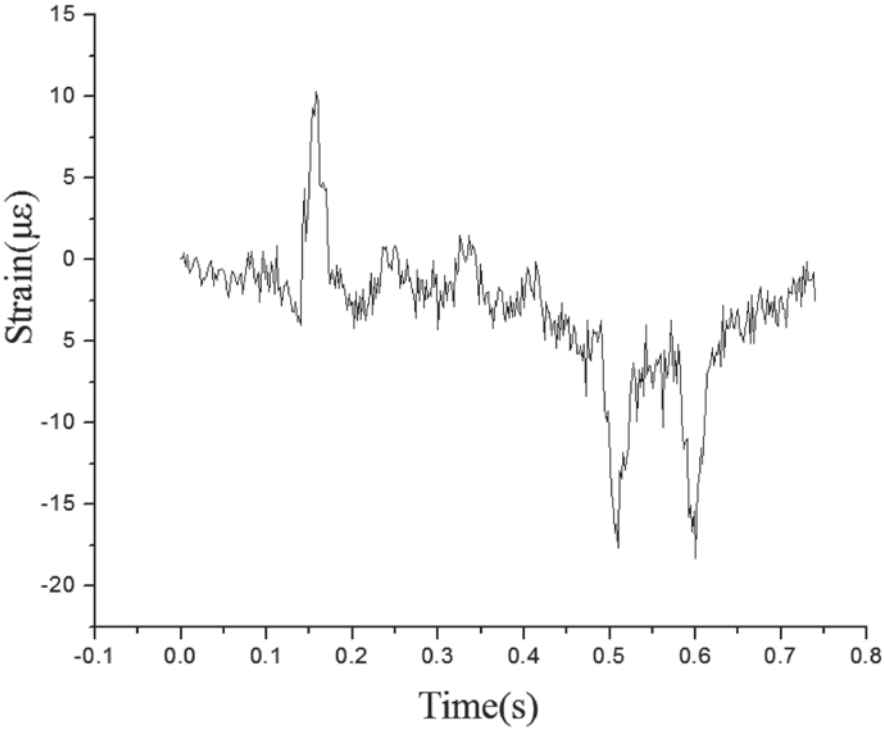

Fig. 10.14 Transverse tensile strain at the bottom of asphalt concrete (simulation)

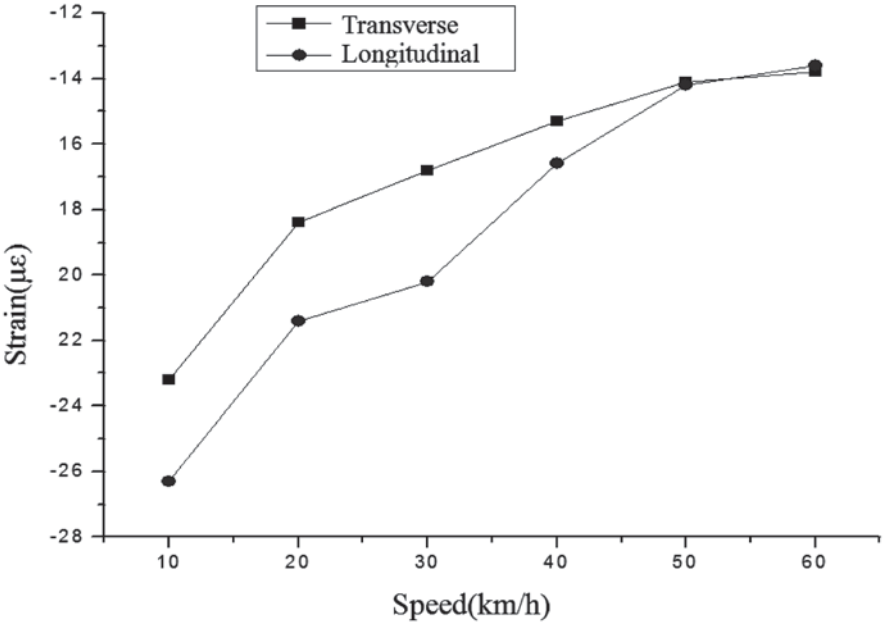

Fig. 10.15 Maximum longitudinal and transverse strain at different vehicle speeds (experiment)

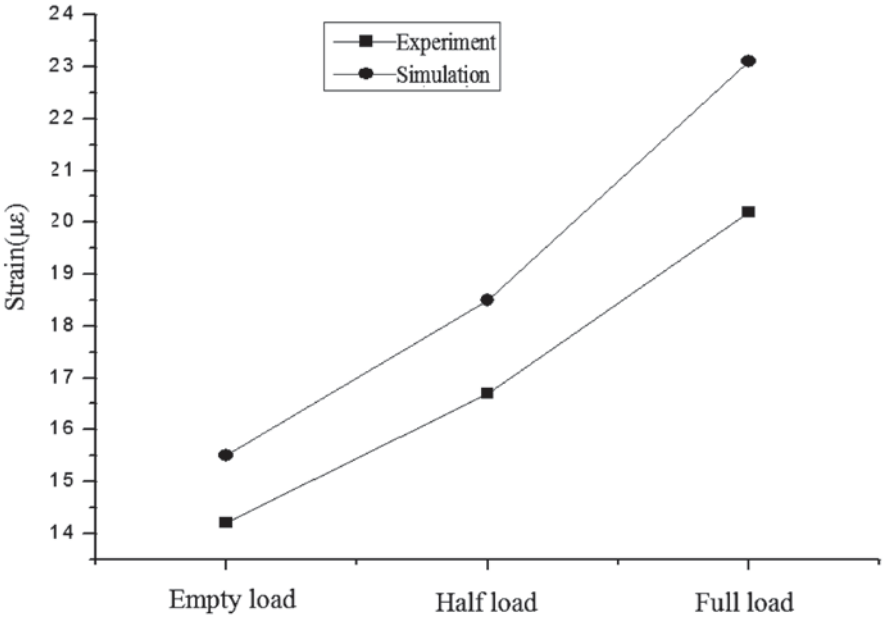

Fig. 10.16 Longitudinal strain comparison between experiment and simulation

transverse strains at the bottom of the surface layer decrease continuously. When the vehicle speed increases from 10 to 30 km/h, the longitudinal tensile strain of the road surface decreases 23.2% while the transverse compressive strain is reduced 27.5%. The reduced magnitude of the longitudinal strain is larger than the transverse strain when the speed is over 30 km/h.

2. Road dynamic strain under different loads

At a speed of 30 km/h under different loading conditions, the tested longitudinal strain results at the bottom of the asphalt concrete are compared with the simulation results, shown in Fig. 10.16. It shows that the longitudinal tensile strain increases with an increase in load. The pattern of the experiment and simulation is the same, and the maximum relative error is 14.3%.

10.4.2 Analysis of Road Vertical Dynamic Stress

1. Vertical dynamic stress of the road at different speeds

Under the condition of a full load, at a speed of 10 km/h, the experimental and simulation results of the vertical dynamic stress at the bottom of the asphalt concrete layer are shown in Figs. 10.17 and 10.18. The experimental and simulation results show the same pattern. The maximum tested compressive stress is −139 kPa and

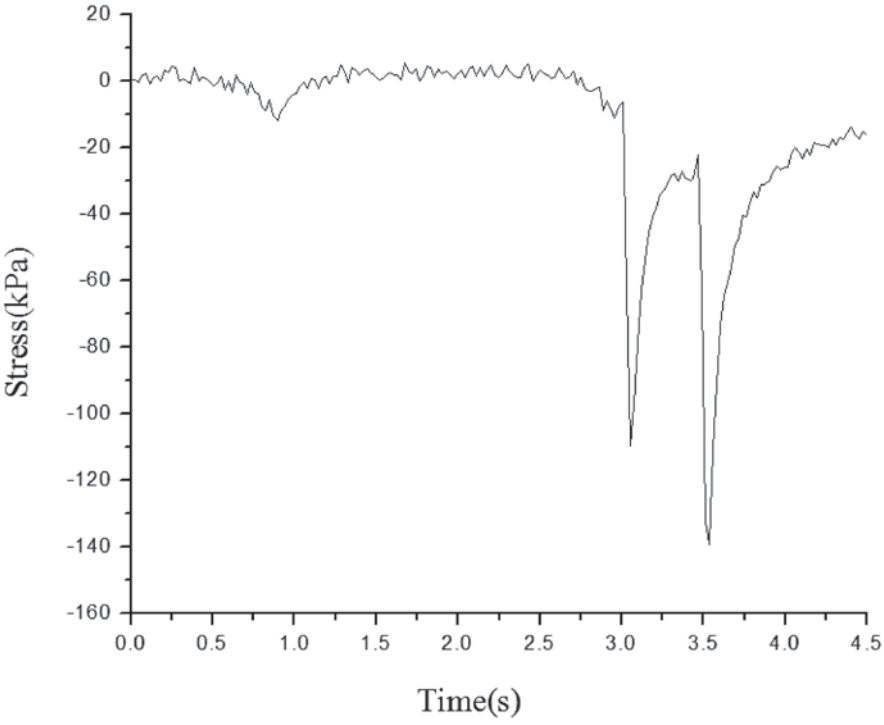

Fig. 10.17 Vertical dynamic stress at the bottom of the asphalt concrete (experiment)

the simulation result is −163 kPa. The relative error is 14.7%, which shows that the simulation result is consistent with the experiment result.

Under the condition of a full load with a respective speed of 10, 20, 40, 60 km/h, the curve is mapped on the basis of the maximum vertical dynamic stress, shown in Fig. 10.19.

Figures 10.17–10.19 show that, under a constant vehicle load, the bottom of the asphalt concrete layer bears vertical compression. Under the same axle load, the compressive stress at the bottom of the surface decreases with an increase in vehicle speed.

2. Vertical dynamic stress of the road under different loads

Under different loading conditions with a constant speed of 30 km/h, the curve of the maximum vertical dynamic stress at the bottom of the asphalt concrete layer is plotted in 10.20. It can be seen that the vertical compressive stress increases with an increase in load, and it presents an approximate linear relationship.

3. Road vertical compressive stress of different structural layers

Under the working condition of a full load and a speed of 60 km/h, the time history curves of the vertical dynamic stress of each road layer are shown in Fig. 10.21. The maximum vertical dynamic stress is shown in Fig. 10.22.

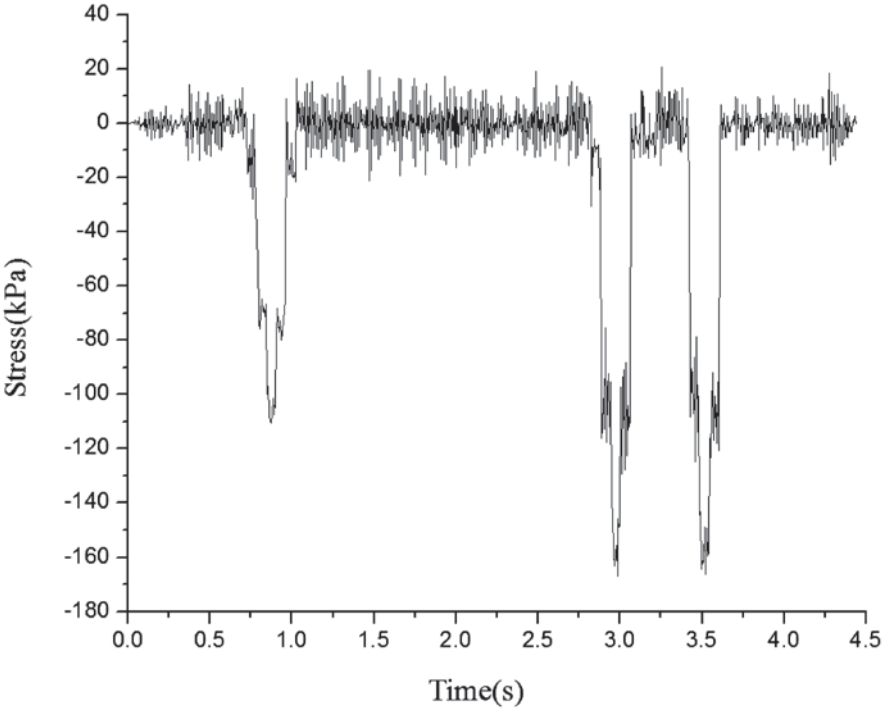

Fig. 10.18 Vertical dynamic stress at the bottom of the asphalt concrete (simulation)

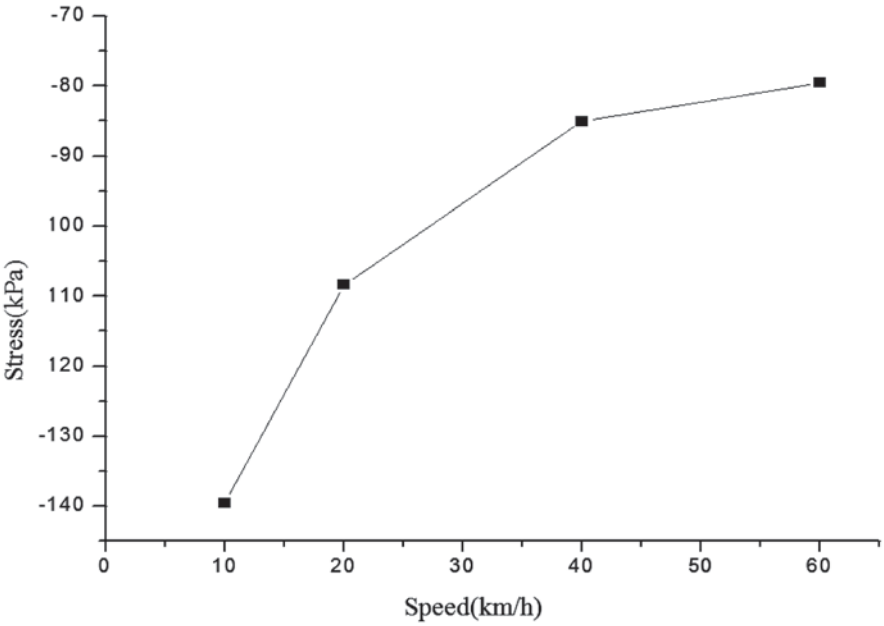

Fig. 10.19 Maximum vertical dynamic stress at different vehicle speeds (experiment)

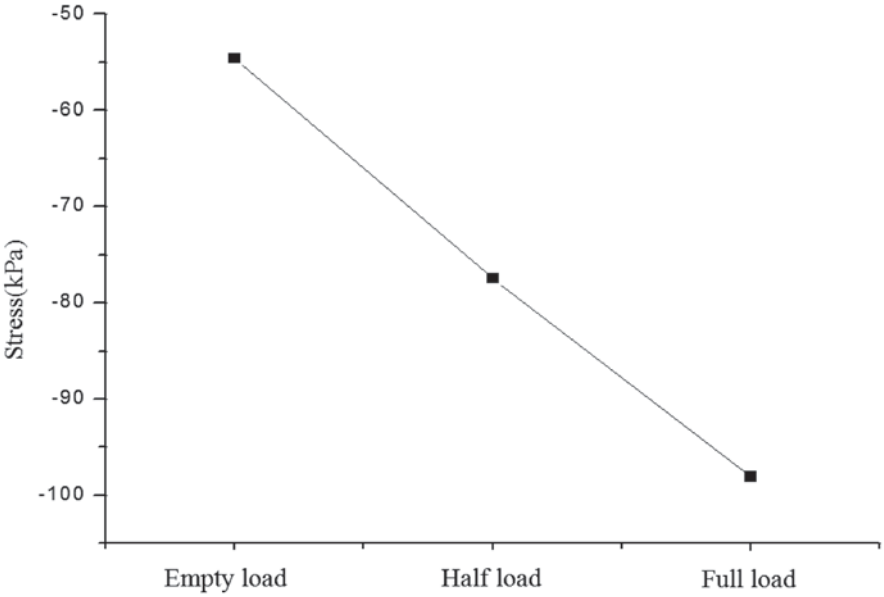

Fig. 10.20 Maximum vertical dynamic stress under different loading (experiment)

Some conclusions can be obtained from Figs. 10.21 and 10.22:

1. Under different vehicle loads, the vertical compressive stress of different road layers continuously decreases with an increase in depth, but its distribution range increases gradually. This conclusion is consistent with the results of previous researches [12, 13].
2. The vertical compressive stress decays quickly in the road structural layers. It reduced 46.7% from the bottom of the asphalt concrete to the bottom of the asphalt treated base layer. The dynamic stress of the cement bound granular layer is very small. Thus, the vertical compressive stress is mainly borne by the asphalt concrete layer. The semi-rigid base can be used to greatly reduce the vertical dynamic stress, which can improve the bearing capacity of the road structure.

10.5 Analysis of the Vehicle Test Results

Under the conditions of empty load, half load, and full load, the vehicle travels at a constant speed of 10, 20, 30, 40, 50, 60 km/h separately on the test section (Class-B road). The curves of vertical acceleration measured from the different points of the

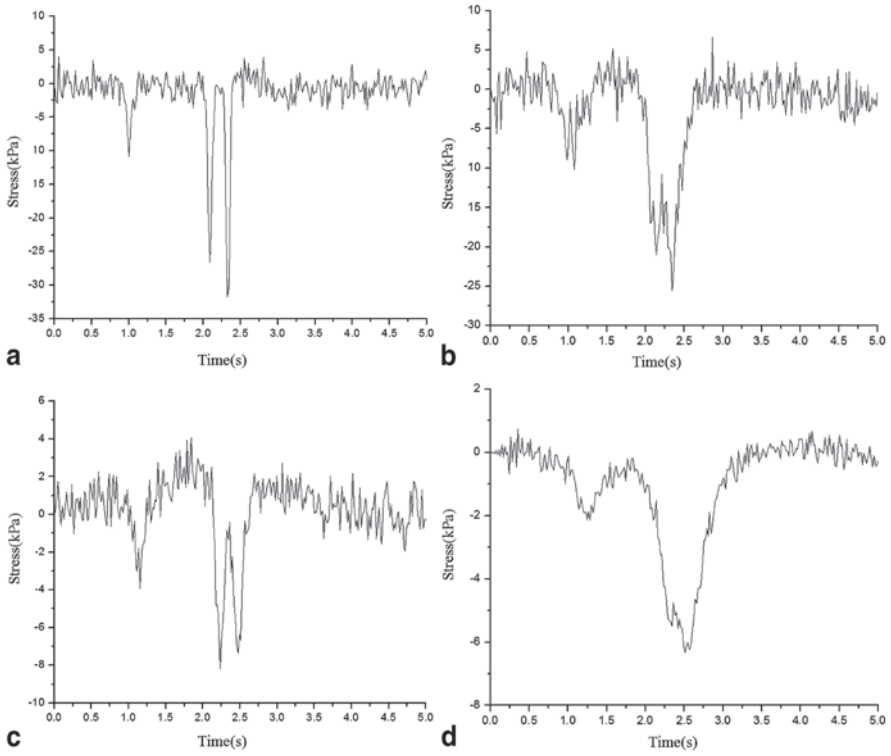

Fig. 10.21 Vertical dynamic stress of different road structure layers. **a** Dynamic stress at the bottom of the asphalt treated base layer. **b** Dynamic stress at the bottom of the upper cement bound granular layer. **c** Dynamic stress at the bottom of the lower cement bound granular layer. **d** Dynamic stress of the upper soil base

vehicle are plotted in Figs. 10.23–10.26. It can be observed that the vehicle vertical acceleration of each measuring point shows an increasing trend. So the working condition of high speed and being overloaded will be unfavorable to the vehicle's riding comfort.

Under the condition of a full load with a speed of 60 km/h, the time domain results of the experiment and the simulation are compared, as shown in Figs. 10.27–10.30. The vehicle simulation model adopts the virtual prototype model from chapter one. The dynamic simulation analysis of the vehicle model is carried out on a random road surface. The default gear stiff integrator (GSTIFF) is adopted to solve the coupled nonlinear differential-algebraic equations (DAE). Through the

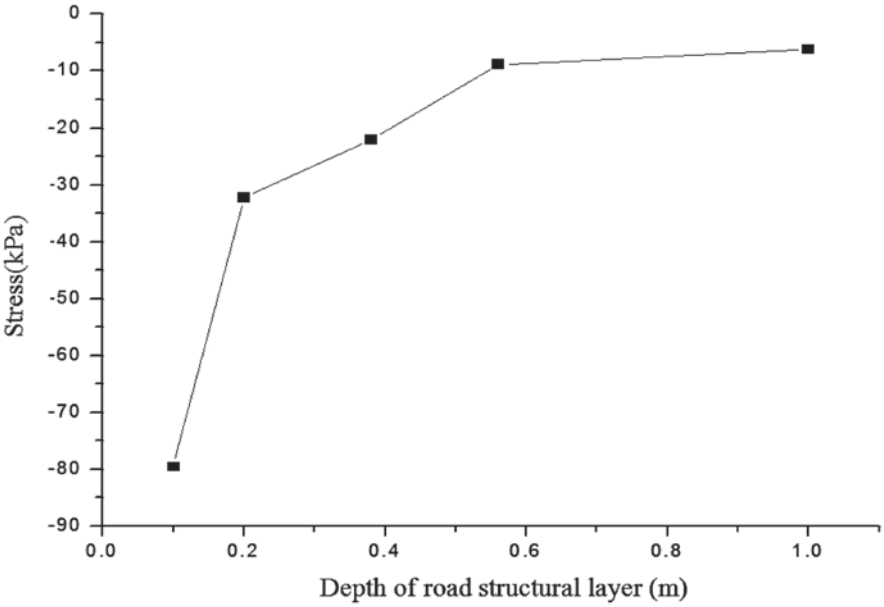

Fig. 10.22 Maximum dynamic stress of each road layer

Fig. 10 23 Vertical acceleration of the driver cab at different speeds and vehicle loads

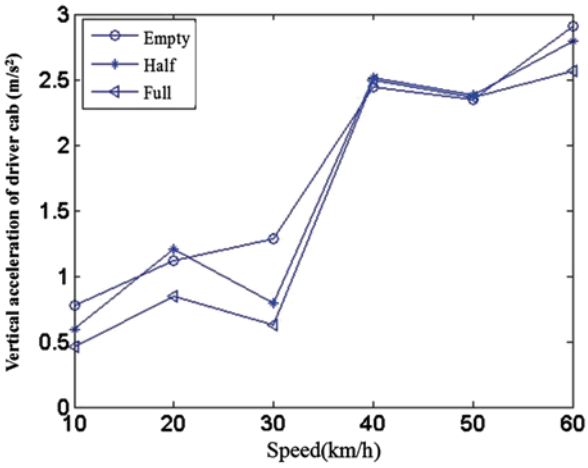

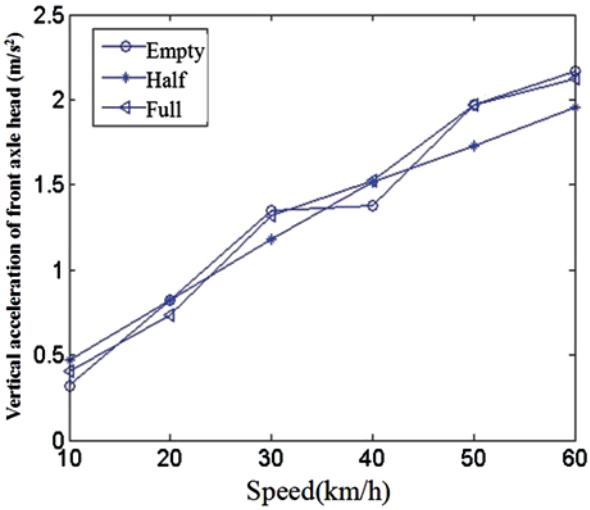

Fig. 10.24 Vertical acceleration of the front axle head at different speeds and loads

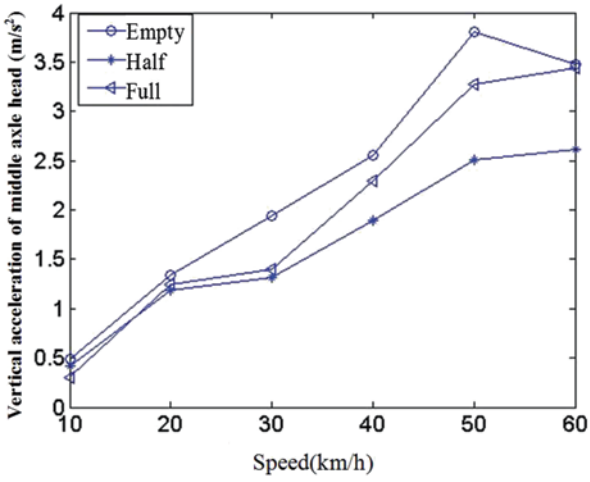

Fig. 10.25 Vertical acceleration of the middle axle head at different speeds and loads

contrasting of Figs. 10.27–10.30, it can be seen that the results of the time trend and distribution of the experiment and simulation are the same.

In order to compare the experimental and simulation results in the time domain and the frequency domain, the acceleration signals are analyzed by utilizing fast Fourier transform (FFT) and a Hanning window is applied to all spectral analyses to inhibit frequency leakage.

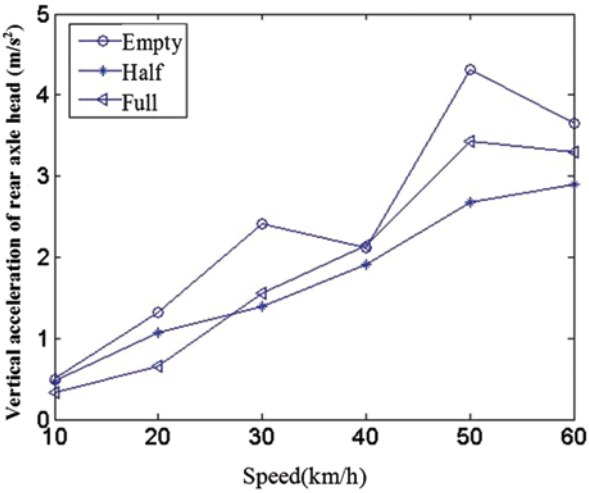

Fig. 10.26 Vertical acceleration of the rear axle head at different speeds and loads

The results of the simulation and the experiment are compared in Table 10.1.

As seen from Table 10.1, the main peak frequency and the amplitude of the simulation results and test results are basically identical. But there are some differences: the maximum relative error of the peak frequency of the power spectral density is 11 % and the maximum relative error of the RMS acceleration is 17 %. In short, the overall trend of simulation results and test results are consistent.

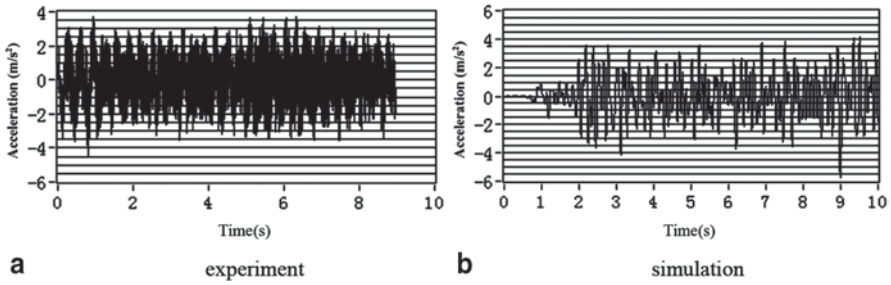

Fig. 10.27 Vertical acceleration of the driver cab in the time domain. **a** experiment. **b** simulation

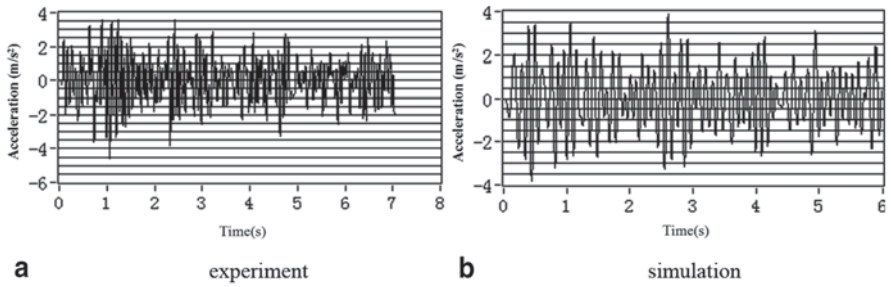

Fig. 10.28 Vertical acceleration of the front axle head in the time domain. **a** experiment. **b** simulation

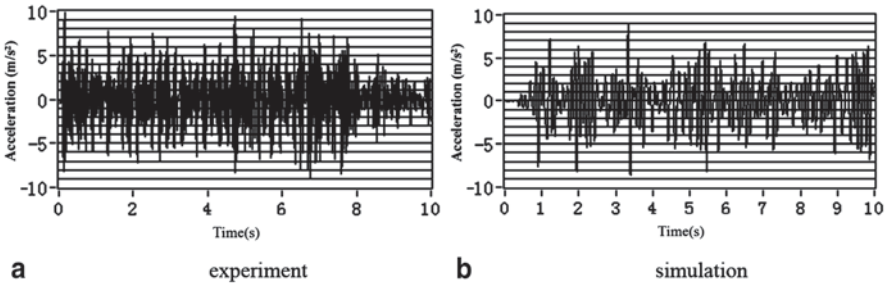

Fig. 10.29 Vertical acceleration of the middle axle head in the time domain. **a** experiment. **b** simulation

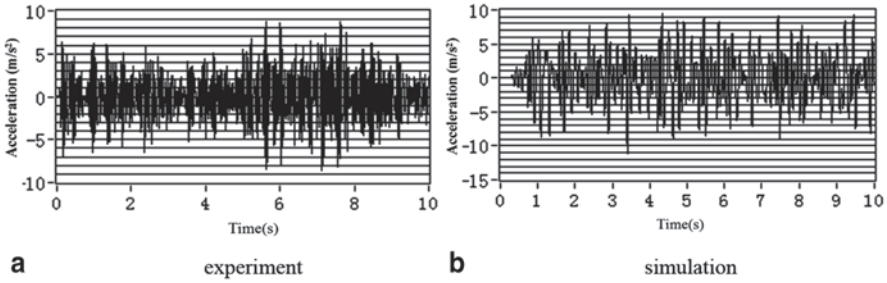

Fig. 10.30 Vertical acceleration of the rear axle head in the time domain. **a** experiment. **b** simulation

Table 10.1 Comparison of the results (experiment and simulation)

Measuring point	Peak frequency of power spectral density(Hz)		RMS of acceleration (m/s^2)	
	Simulation	Experiment	Simulation	Experiment
Driver cab	3.82	3.39	2.12	2.57
Front axle head	10.81	9.98	2.19	1.97
Middle axle head	9.60	10.00	3.51	3.14
Rear axle head	10.01	10.10	3.50	3.37

10.6 Chapter Summary

In order to reveal comprehensively the failure characteristics and the asphalt pavement structure, a section of an expressway is built as a test section. The specific methods of arrangement of different kinds of sensors are put forward for various layers of the road. Based on the test section of the vehicle–road system, the dynamic response data of the vehicle and the road are acquitted. The transverse stress, the longitudinal stress, the dynamic pressure, and the static pressure of each road layer

are collected in details. It provides significant data for the analysis of the dynamic interaction between a vehicle and a road.

References

1. Huang YX. Pavement analysis and design. Beijing: People's Communications Press; 1998.
2. Sun LJ. Structural behavior theory of asphalt pavement. Beijing: People's Communications Press; 2005.
3. Kumara MW, Tia M, Bergin M. Evaluation of early strength requirement of concrete for slab replacement using accelerated pavement testing. J Transp Eng. 2006;132(10):781–9.
4. Qian ZD, Zhang L, Chen LL. Pavement structural dynamics. Najing: Southeast University Press; 2010.
5. Potter TEC, Cebon D, Cole DJ. An investigation of road damage due to measured dynamic tire forces. Proc Inst Mech Eng Part D, J Automob Eng. 1995;209(1):9–24.
6. Pei JZ. Microstructural properties and decay behavior of asphalt pavement. Science Press; 2010.
7. Hunaidi O, Guan W, Nicks J. Building vibrations and dynamic pavement loads induced by transit buses. Soil Dyn Earthq Eng. 2000;19(64):435–45.
8. Dong ZJ, Liu H, Tan YQ. Field measurement of three-directional strain response of asphalt pavement. JSCUT. 2009;(7):46–51.
9. Jeongho O, Fernando EG, Lytton RL. Evaluation of damage potential for pavements due to overweight truck traffic. J Transp Eng. 2007;133(5):308–17.
10. Kim SM, Roesset JM. Moving loads on a plate on an elastic foundation. J Eng Mech. 1998;124(9):1010–17.
11. Lv PM. Mechanical analysis of vehicle-asphalt pavement. Beijing: People's Communications Press; 2010.
12. Kim SM, Mccullough BF. Dynamic response of a plate on a viscous Winkler foundation to moving loads of varying amplitude. Eng Struct. 2003;25(9):1179–88.
13. Kim SM. Influence of horizontal resistance at plate bottom on vibration of plates on an elastic foundation under moving loads. Eng Struct. 2004;26:519–29.